

A study of nuclear radii and neutron skin thickness of neutron-rich nuclei near the neutron drip line

Usuf Rahaman, M. Ikram, M. Imran, Anisul Ain Usmani

Department of Physics, Aligarh Muslim University, Aligarh-202002, India

Abstract

We studied the charge radius (r_c), neutron radius (r_n), and neutron skin-thickness ($\Delta r = r_n - r_p$) over a chain of isotopes from C to Zr with the stable region to the neutron drip line. Theoretical calculations are done with axially deformed self-consistent relativistic mean-field theory (RMF) with effective nonlinear NL3 and NL3* interactions. The theoretically estimated values are compared with available experimental data and a reasonable agreement is noted. We additionally assessed the two-neutron separation energy (S_{2n}) to mark the drip line nuclei of the considered isotopic series. In the reference of S_{2n} , neutron magicity is also discussed. The calculated neutron radii are compared with empirical estimation made by $r = r_0 N^{1/3}$ to examine the abnormal trend of the radius for neutron drip line nuclei. In view to guide the long tails, the density distribution for some skin candidates is analyzed. Finally, neutron skin thickness is observed for the whole considered isotopic series.

PACS: 21.10.k, 21.10.Dr, 21.10.Ft, 21.10.Gv, 21.60.n

Keywords: Relativistic mean-field (RMF) theory; Skin thickness; Neutron-rich nuclei.

1 Introduction

The study of exotic neutron-rich nuclei has gained worldwide attention because of their unexpected behaviour such as nuclear halo and skin [1–3]. These phenomena are supposed to be significant characteristics of the nuclei at the extreme [2, 3]. The pieces of information gathered from such nuclei are used for astrophysical studies to understand the origin of heavy elements. The exotic nuclei having excessive number of neutrons possess larger N/Z ratios than the β stable nuclei. These excessive neutrons in neutron-rich nuclei are responsible to produce a huge contrast in Fermi energy of neutrons and protons, in turn, making a decoupling between neutron and proton distribution and as a result, nuclear skin structure is formed.

In past few years, a large number of theoretical studies have been conducted to determine the nature of the neutron distribution in exotic neutron-rich nuclei [4–8]. Agbemava *et al.* has made recent progress on neutron drip line nuclei within the RMF model using several parameterizations in axially manner [6]. The investigations have been used for global assessment of the accuracy of the description of nuclear structure phenomena especially ground-state properties of even-even nuclei and also to describe the location of two-proton as well as two-neutron drip lines. Moreover, Xia *et al.* also calculated the ground-state properties of nuclei with $8 \leq Z \leq 120$ using the spherical relativistic continuum Hartree-Bogoliubov method [7]. They described that there are 9035 nuclei predicted to be bound by incorporating the continuum effect which largely extends the existing nuclear landscapes. They demonstrated that the coupling between the bound states and the continuum due to the pairing correlations plays an essential role in extending the nuclear landscape. In continuation of the above work, K. Zhang *et al.*, made the description of even-even nuclei in the nuclear chart in an axially deformed manner based on point coupling method [8]. In Ref. [7], the work is done for a wide range of nuclear chart within spherical symmetry but the present investigations have to be made for axially symmetric cases whereas a point coupling method is used in Ref. [8]. Moreover, present work is also devoted to all even-odd, odd-even, odd-odd, and even-even systems. Therefore, it has significance in nuclear structure phenomena especially the nuclear skin structure of exotic nuclei.

It merits referencing that the density distributions of exotic neutron-rich nuclei are quite different from the nuclei reside at the stability line. The profile of neutron density is supposed to be extended beyond the proton den-

sity as the excessive neutrons are pushed out against the nuclear surface and therefore creating a sort of neutron skin. The neutron skin thickness is characterized as $\Delta r = r_n - r_p$ with r_n and r_p being the root mean square (RMS) radii for the neutron and proton distributions, respectively. The development of neutron skin on the surface of a nucleus is a marvel of enthusiasm for nuclear structure physics to represents the rudimental nuclear properties of nuclei. The neutron skin thickness depends mainly on the balancing condition between the isospin asymmetry and the Coulomb force. Thus, the skin is responsible enough to look at the isovector properties while our understanding of isovector density ($\rho_1 = \rho_n - \rho_p$) is poorly known. However, in the mean-field estimations, the skin thickness is identified with the divergence in the Fermi energies among protons and neutrons. The main perception on neutron skin with a thickness of 0.9 fm was accounted for by Tanihata *et al.* [9] in He nucleus, and later was additionally affirmed by G. D. Alkharov *et al.* [10].

Reliable theoretical calculations regarding neutron skin are quite essential not only to describe the structure of neutron-rich nuclei but also for modeling the neutron-rich matter. In recent years, a large number of theoretical studies have been conducted to determine the nature of the neutron distribution in exotic neutron-rich nuclei [11–14]. The relativistic calculations on neutron skin thickness have been made for the ^{208}Pb nucleus and its relationship with the slope of symmetry energy has been examined [15–21]. Apart from theoretical investigations, the recent Lead Radius EXperiment (PREX) has now established the existence of a neutron skin for the ^{208}Pb nucleus in a clean and model-independent way with a high level of accuracy [22]. Moreover, new experimental programs using both stable and exotic beams at various laboratories such as JLab, FAIR, FRIB, MESA, and RIKEN are in progress and the data are awaited concerned to the nuclear structure studies in order to find the answers of some fundamental questions over the neutron skin thickness [23].

Neutron skin thickness of neutron-rich nuclei is intently related to density dependence of symmetry energy and a significant discernible for testing the symmetry potential of nuclear matter [2, 3]. Neutron skin plays a significant role in correlation with several physical observable over the finite nuclei, nuclear symmetry energy and infinite nuclear matter to pure neutron matter [16–21, 24–28]. The determination of the neutron skin thickness for finite nuclei is supposed to be a unique experimental constraint on the symmetry energy. Skin varies linearly with the slope parameter (L) of density depen-

dence of the nuclear symmetry energy at saturation density and it can probe the isovector part of the nuclear interaction [16]. Moreover, it is also beautifully linked with the various constraint found to force on the neutron equation of state (EOS) of high-density matter in neutron stars [17–21, 25]. The EOS has a significant impact on neutron star structure modeling [18, 29–32]. Despite many efforts in infinite many-body systems, our knowledge of density dependence of the symmetry energy is still very limited [16–21]. Nuclear symmetry energy can not be measured directly within the available nuclear experimental facilities but the information about it tends to be picked up by the assurance of either the neutron skin of neutron-rich nuclei or the radii of neutron stars [16–21]. In this way, predictions on neutron skin might be useful to fix the constraint on the calculation of symmetry energy of infinite nuclear matter or pure neutron matter which in turn can be used to simulate the mass and radius of the neutron star. In this regard, we endorse a measurement of the neutron skin thickness of the neutron-rich nuclei from C to Zr isotopes.

In this paper, we make a theoretical investigation for neutron skin for a series of neutron-rich nuclei from C to Zr isotopes. The present calculations are performed within self-consistent axially deformed relativistic mean-field model with effective NL3 and NL3* parameter sets. The physical observable of interest are root mean square charge radius, neutron radius, neutron skin thickness, separation energy and density distributions of protons and neutrons. In this work, the drip line signifies the two-neutron drip line calculated by two neutron separation energy. Moreover, the exposure of the closed shell of the nuclei are also discussed on the basis of two-neutron separation energy. The paper is arranged in the following way: Section one contains the introduction of the manuscript. The used formalism relativistic mean-field model is expressed in section two. Results are given in section three. Finally, the manuscript is summarized and concluded in section four.

2 Theoretical Formalism

The RMF theory has made incredible progress in portraying the nuclear many-body problem and also explained the numerous nuclear phenomena over the whole periodic table [33–40]. It is very better to get the spin orbit splitting automatically over the non-relativistic case which gains us to understand the closed shell structure of the nuclei [41, 42]. The RMF theory

starts with the fundamental Lagrangian density containing nucleons interacting with σ -, ω -, and ρ -meson fields. The photon field A_μ is incorporated to deal with the Coulomb interaction of protons. The Lagrangian density for the relativistic mean-field theory is represented as [33–37],

$$\begin{aligned}
\mathcal{L} &= \bar{\psi}_i \{ i\gamma^\mu \partial_\mu - M \} \psi_i + \frac{1}{2} \partial^\mu \sigma \partial_\mu \sigma - \frac{1}{2} m_\sigma^2 \sigma^2 - \frac{1}{3} g_2 \sigma^3 \\
&- \frac{1}{4} g_3 \sigma^4 - g_s \bar{\psi}_i \psi_i \sigma - \frac{1}{4} \Omega^{\mu\nu} \Omega_{\mu\nu} + \frac{1}{2} m_\omega^2 V^\mu V_\mu \\
&- g_\omega \bar{\psi}_i \gamma^\mu \psi_i V_\mu - \frac{1}{4} \vec{B}^{\mu\nu} \vec{B}_{\mu\nu} + \frac{1}{2} m_\rho^2 \vec{R}^\mu \vec{R}_\mu - \frac{1}{4} F^{\mu\nu} F_{\mu\nu} \\
&- g_\rho \bar{\psi}_i \gamma^\mu \vec{\tau} \psi_i \vec{R}^\mu - e \bar{\psi}_i \gamma^\mu \frac{(1 - \tau_{3i})}{2} \psi_i A_\mu.
\end{aligned} \tag{1}$$

Here M , m_σ , m_ω , and m_ρ are the masses for nucleons, σ -, ω -, and ρ -mesons, and ψ is its Dirac spinor. The field for the σ -meson is denoted by σ , ω -meson by V_μ and ρ -meson by R_μ . g_s , g_ω , g_ρ and $e^2/4\pi = 1/137$ are the coupling constants for the σ -, ω -, ρ -mesons, and photon respectively. g_2 and g_3 are the self-interaction coupling constants for σ -mesons. By utilizing the classical variational principle, we get the field equations for the nucleons and mesons. The Dirac equation for the nucleons is inscribed by

$$\{ -i\alpha \nabla + V(r_\perp, z) + \beta M^\dagger \} \psi_i = \epsilon_i \psi_i. \tag{2}$$

The effective mass of the nucleons is

$$M^\dagger = M + S(r_\perp, z) = M + g_\sigma \sigma^0(r_\perp, z), \tag{3}$$

and the vector potential is

$$V(r_\perp, z) = g_\omega V^0(r_\perp, z) + g_\rho \tau_3 R^0(r_\perp, z) + e \frac{(1 - \tau_3)}{2} A^0(r_\perp, z). \tag{4}$$

The field equations for mesons are given by

$$\begin{aligned}
\{ -\Delta + m_\sigma^2 \} \sigma^0(r_\perp, z) &= -g_\sigma \rho_s(r_\perp, z) \\
&- g_2 \sigma^2(r_\perp, z) - g_3 \sigma^3(r_\perp, z),
\end{aligned} \tag{5}$$

$$\{ -\Delta + m_\omega^2 \} V^0(r_\perp, z) = g_\omega \rho_v(r_\perp, z), \tag{6}$$

$$\{ -\Delta + m_\rho^2 \} R^0(r_\perp, z) = g_\rho \rho_3(r_\perp, z), \tag{7}$$

$$-\Delta A^0(r_\perp, z) = e \rho_c(r_\perp, z). \tag{8}$$

The meson field σ^0 , V^0 , R^0 are only the time dependent component of the meson field. These components come into play when time reversal symmetries are taken into consideration for solving the field equations. Under time reversal, the spatial components of meson fields are omitted. As we know that relativistic quantities have four components; 1-time and 3-spatial ($i = 0, 1, 2, 3$). As the time reversal symmetry is used, the spatial component has been eliminated and therefore only the time component is used to play which is denoted by $i = 0$ and therefore meson fields are denoted by σ^0 , V^0 , R^0 .

Here, $\rho_s(r_\perp, z)$, and $\rho_v(r_\perp, z)$ are the scalar and vector density for σ - and ω -fields in a nuclear system and represented as

$$\begin{aligned}\rho_s(r_\perp, z) &= \sum_{i=n,p} \bar{\psi}_i(r) \psi_i(r) , \\ \rho_v(r_\perp, z) &= \sum_{i=n,p} \psi_i^\dagger(r) \psi_i(r) .\end{aligned}\tag{9}$$

These equations of motion are solved to acquire a static solution for the nuclei to deduce their ground state properties. The set of nonlinear coupled equations are solved self-consistently in an axially deformed harmonic oscillator basis $N_F = N_B = 14$ for fermion and boson basis. The radii are calculated from the corresponding densities

$$\begin{aligned}\langle r_p^2 \rangle &= \frac{1}{Z} \int r^2 d^3r \rho_p(r_\perp, z) , \\ \langle r_n^2 \rangle &= \frac{1}{N} \int r^2 d^3r \rho_n(r_\perp, z) , \\ \langle r_m^2 \rangle &= \frac{1}{A} \int r^2 d^3r \rho(r_\perp, z) ,\end{aligned}\tag{10}$$

for proton, neutron, and matter rms radii, respectively. The quantities ρ_p , ρ_n , and ρ are their relating densities. The charge rms radius can be calculated from the proton rms radius utilizing the standard expression [43, 44]

$$\langle r_c^2 \rangle = \langle r_p^2 \rangle + R_p^2 + \frac{N}{Z} R_n^2 + \frac{3h^2}{4m_p^2 c^2},\tag{11}$$

where $3h^2/4m_p^2 c^2 \simeq 0.033\text{fm}^2$, $R_n^2 = -0.1149(27)\text{fm}^2$, $R_p = 0.8775(51)\text{fm}$.

The quadrupole deformation parameter β_2 is extracted from the calculated quadrupole moments of neutrons and protons through

$$Q = Q_n + Q_p = \sqrt{\frac{16\pi}{5}} \left(\frac{3}{4\pi} AR^2 \beta_2 \right), \quad (12)$$

where $R = 1.2A^{1/3}$.

The total energy of the system is given by

$$E_{total} = E_{part} + E_{\sigma} + E_{\omega} + E_{\rho} + E_c + E_{pair} + E_{c.m.}, \quad (13)$$

where E_{part} is the sum of the single particle energies of the nucleons and E_{σ} , E_{ω} , E_{ρ} , E_c , E_{pair} , $E_{c.m.}$ are the contributions of the meson fields, the Coulomb field, pairing energy, and the center-of-mass energy, respectively.

In present calculations, the non-linear NL3 [45] and NL3* [46] parameterizations are used throughout the calculations. In Table 1, we have listed the masses, coupling constants for nucleons and mesons for both NL3 and NL3* effective force parameterization sets. The properties of nuclear matter for the same parameterizations are also framed in the Table 1. For detailed formalism and numerical techniques, it is recommended to follow the Refs. [49, 50] and the references therein. It is known that consideration of pairing is important for open shell nuclei. Thus, constant gap BCS approximation is used to take care of pairing interaction as given in Ref. [51]. In the case of simple BCS prescription, the expression of pairing energy is written by

$$E_{pair} = -G \left[\sum_{i>0} u_i v_i \right]^2, \quad (14)$$

where G is the pairing force constant, and v_i^2 and $u_i^2 = 1 - v_i^2$ are the occupation probabilities. The variation with respect to the occupation numbers, v_i^2 , is expressed by the well-known BCS equation

$$2\epsilon_i u_i v_i - \Delta(u_i^2 - v_i^2) = 0, \quad (15)$$

with $\Delta = G \sum_{i>0} u_i v_i$. The occupation number n_i is given by

$$n_i = v_i^2 = \frac{1}{2} \left[1 - \frac{\epsilon_i - \lambda}{\sqrt{(\epsilon_i - \lambda)^2 + \Delta^2}} \right], \quad (16)$$

where ϵ is the single-particle energy for the state i . The chemical potential λ for protons (neutrons) is obtained requiring

$$\sum_i n_i = Z(N). \quad (17)$$

The sum is taken over proton (neutron) states. The value of constant gap (pairing gap) for proton and neutron are determined from the phenomenological formula of Madland and Nix [51] which are given as

$$\Delta_n = \frac{r}{N^{1/3}} \exp(-sI - tI^2), \quad (18)$$

and

$$\Delta_p = \frac{r}{Z^{1/3}} \exp(-sI - tI^2), \quad (19)$$

where $I = (N - Z)/A$, $r = 5.73$ MeV, $s = 0.117$, and $t = 7.96$. In particular, for the solution of the RMF equations with pairing, we never calculate the pairing force constant G explicitly. But the occupation probabilities are directly calculated using the gap parameters (Δ_n and Δ_p) and the chemical potentials (λ_n and λ_p) for neutrons and protons, while chemical potentials are determined by the numbers of protons and neutrons. And now, the expression of pairing energy is simplified to

$$E_{pair} = -\Delta \sum_{i>0} u_i v_i. \quad (20)$$

The centre-of-mass correction is included by non relativistic expression i.e. $E_{c.m.} = -\frac{3}{4}41A^{-1/3}$.

Moreover, it is not enough to compute the binding energy and quadrupole moment of odd- N or odd- Z or both odd- N and odd- Z systems in the present model due to mean-field approach. Therefore, we use the Pauli blocking approximation to take care of the time reversal symmetry in the mean-field model and pursued our calculations in this context. The blocking approximation restores the time-reversal symmetry and as a result, reveals the even-odd staggering very nicely, but doubles our effort as we need to perform our calculations twice [52, 53].

3 Results and discussions

In this manuscript, we played out a self-consistent axially deformed relativistic mean-field calculation to find out the binding energy, radii, quadrupole

Table 1: The NL3 [45] and NL3* [46] force parameter sets and their corresponding nuclear matter properties [45–48] are listed here.

parameters		NL3	NL3*
M (MeV)		939	939
m_σ (MeV)		508.194	502.5742
m_ω (MeV)		782.501	782.6
m_ρ (MeV)		763	763
g_σ		10.217	10.0944
g_ω		12.868	12.8093
g_ρ		4.474	4.5748
g_2 (fm ⁻¹)		-10.4307	-10.8093
g_3		-28.8851	-30.1486
Nuclear matter properties			
ρ_o (fm ⁻³)	(Saturation density)	0.148	0.15
$(E/A)_\infty$ (MeV)	(Infinite nuclear matter binding energy)	-16.29	-16.31
m^*/m	(Ratio of effective mass and bare mass)	0.595	0.594
K (MeV)	(Incompressibility)	271.5	258.27
$J=S(\rho_0)$ (MeV)	(Saturation density)	37.4	38.68
L (MeV)	(Slope of S)	118.65	122.63
K_{sym} (MeV)	(Curvature of S)	101.34	105.56

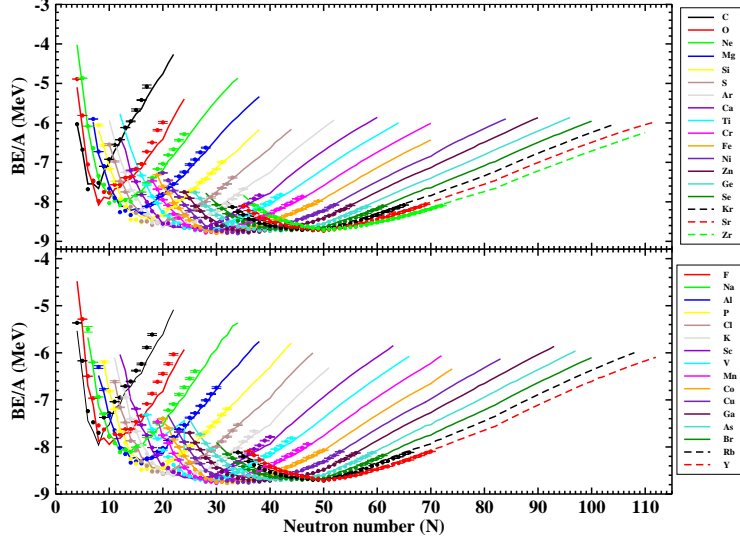


Figure 1: (color online) Binding energy per particle (BE/A) calculated using RMF theory with NL3 parameterization, is plotted as a function of neutron number for nuclei from C to Zr. Experimental data are represented by filled circles. Even- Z nuclei on the upper panel and odd- Z nuclei are given on the lower panel.

deformation parameter, and density distributions. Two-neutron separation energy and skin-thickness are estimated from the calculated binding energies and radii, respectively. Both separation energy and neutron radius are supposed to be crucial parameters to determine the halo or skin structure of neutron-rich exotic nuclei. And, thus the determination of nuclear skin within the considered isotopic series is the main objective of our manuscript. Further to guide the view of long tails, the nucleons density distribution is analyzed. We also discuss the appearance of closed shell within the considered nuclei. All the results in the forms of tables and figures are explained in forthcoming subsections.

3.1 Binding energy and separation energy

The calculated binding energy in terms of binding energy per particle (BE/A) and two-neutron separation energies of the isotopic chain from carbon to zirconium isotopes are plotted in Figs. 1-6 with NL3 and NL3* parameter-

Table 2: The quantities nuclear asymmetry parameter ($\delta=N - Z/A$), BE/A(MeV), S_{2n} (MeV), β_2 and Δr (fm), calculated using RMF theory with NL3 parameterization, are listed for two neutron drip line nuclei.

Nuclei	δ	BE/A	S_{2n}	β_2	Δr	Nuclei	δ	BE/A	S_{2n}	β_2	Δr
²³ C	0.478	5.373	2.009	0.062	0.934	²⁷ N	0.481	5.613	2.392	0.005	0.884
²⁹ O	0.448	6.121	0.394	0.043	0.887	³⁰ F	0.400	6.598	1.638	0.045	0.744
³⁴ Ne	0.459	5.928	0.760	0.498	0.878	³⁹ Na	0.436	6.260	0.833	0.463	0.800
⁴¹ Mg	0.415	6.570	1.407	0.449	0.807	⁴⁸ Al	0.458	6.131	0.711	0.104	0.943
⁴⁹ Si	0.429	6.553	1.468	0.015	0.883	⁵⁵ P	0.455	6.313	1.063	0.006	0.867
⁵⁶ S	0.429	6.650	1.456	0.055	0.801	⁵⁸ Cl	0.414	6.825	0.790	0.075	0.777
⁵⁹ Ar	0.389	7.129	2.279	0.039	0.715	⁶⁰ K	0.367	7.405	3.214	0.003	0.668
⁷³ Ca	0.444	6.522	0.110	0.114	0.864	⁷⁶ Sc	0.447	6.490	0.022	0.127	0.918
⁷⁹ Ti	0.443	6.550	0.134	0.165	0.924	⁸⁰ V	0.425	6.774	0.493	0.207	0.860
⁸⁷ Cr	0.448	6.516	0.131	0.159	0.959	⁹³ Mn	0.462	6.364	0.323	0.094	0.972
⁹⁵ Fe	0.463	6.499	0.042	0.064	0.950	⁹⁷ Co	0.443	6.655	1.689	0.001	0.945
⁹⁸ Ni	0.433	6.847	3.031	0.001	0.901	¹⁰¹ Cu	0.426	6.839	0.126	0.077	0.881
¹⁰⁸ Zn	0.444	6.622	0.177	0.256	0.943	¹¹⁰ Ga	0.436	6.713	0.126	0.249	0.906
¹¹² Ge	0.446	6.808	0.436	0.242	0.981	¹¹⁵ As	0.426	6.825	0.261	0.235	0.862
¹¹⁷ Se	0.419	6.917	0.583	0.007	0.764	¹¹⁸ Br	0.407	7.045	0.756	0.010	0.738
¹²¹ Kr	0.404	7.053	0.218	0.126	0.785	¹²⁶ Rb	0.413	6.945	0.085	0.175	0.865
¹³² Sr	0.424	6.794	0.187	0.174	0.947	¹³⁴ Y	0.418	6.852	0.013	0.245	0.866
¹³⁵ Zr	0.407	6.964	0.325	0.259	0.820						

Table 3: Same as Table 2 but for NL3* parameterization.

Nuclei	δ	BE/A	S_{2n}	β_2	Δr	Nuclei	δ	BE/A	S_{2n}	β_2	Δr
²³ C	0.478	5.306	1.954	0.096	0.945	²⁷ N	0.481	5.561	2.255	0.005	0.897
²⁹ O	0.448	6.067	0.499	0.108	0.907	³⁰ F	0.400	6.488	2.844	0.189	0.745
³⁴ Ne	0.412	6.442	1.907	0.462	0.734	³⁹ Na	0.436	6.208	0.534	0.463	0.815
⁴¹ Mg	0.415	6.514	1.616	0.458	0.774	⁴⁸ Al	0.458	6.078	0.918	0.112	0.955
⁴⁹ Si	0.429	6.499	1.221	0.051	0.893	⁵⁵ P	0.455	6.265	0.815	0.006	0.882
⁵⁶ S	0.429	6.606	1.198	0.055	0.815	⁵⁸ Cl	0.414	6.775	0.597	0.099	0.797
⁵⁹ Ar	0.390	7.088	2.137	0.075	0.720	⁶⁰ K	0.367	7.361	3.381	0.047	0.678
⁷¹ Ca	0.437	6.562	0.030	0.115	0.903	⁷² Sc	0.417	6.797	0.149	0.133	0.811
⁷⁹ Ti	0.443	6.503	0.077	0.158	0.942	⁸⁰ V	0.425	6.728	0.473	0.195	0.880
⁸⁶ Cr	0.442	6.550	0.158	0.159	0.963	⁹⁰ Mn	0.444	6.528	0.041	0.094	0.964
⁹⁵ Fe	0.453	6.454	0.275	0.066	0.949	⁹⁷ Co	0.443	6.614	1.329	0.001	0.964
⁹⁸ Ni	0.429	6.807	2.656	0.002	0.919	¹⁰⁰ Cu	0.420	6.873	0.351	0.077	0.886
¹⁰¹ Zn	0.406	7.025	1.341	0.256	0.837	¹⁰⁹ Ga	0.431	6.732	0.169	0.242	0.919
¹¹² Ge	0.429	6.763	0.438	0.241	0.894	¹¹⁴ As	0.421	6.841	0.164	0.248	0.824
¹¹⁷ Se	0.419	6.863	0.177	0.125	0.789	¹¹⁸ Br	0.407	6.997	0.437	0.063	0.764
¹²¹ Kr	0.405	7.009	0.094	0.126	0.805	¹²⁵ Rb	0.408	6.962	0.110	0.165	0.862
¹³¹ Sr	0.420	6.809	0.012	0.174	0.952	¹³⁴ Y	0.426	6.724	0.035	0.245	1.053
¹³⁵ Zr	0.407	6.923	0.333	0.259	0.968						

Table 4: The possible number of neutron are listed for two-neutron drip line nuclei produced in this work by RMF model with NL3 and NL3* parameterizations. Comparison of present work has been made with prediction of spherical RCHB [7], available experimental data [54] and with macroscopic FRDM data [60]

Nuclei	RMF+NL3	RMF+NL3*	Experiment	RCHB+PC-PK1	FRDM
C	17	17	16		
N	20	20	17		
O	21	21	17		19
F	21	21		23	23
Ne	24	24		32	24
Na	28	28		35	27
Mg	29	29		35	28
Al	35	35		37	29
Si	35	35		39	32
P	40	40		41	35
Se	40	40		41	36
Cl	41	41		42	40
Ar	41	41		45	43
K	41	41		59	46
Ca	53	51		61	49
Sc	55	51		62	50
Ti	57	57		62	51
V	57	57		65	52
Cr	65	64		69	54
Mn	68	65			54
Fe	69	69		71	57
Co	70	70		71	59
Ni	70	70		71	64
Cu	72	71		71	67
Zn	78	71		73	70
Ga	78	78		79	72
Ge	80	80		83	75
As	81	81		85	82
Se	83	83		94	82
Br	83	83		96	82
Kr	85	85		100	83
Rb	89	88	13	102	83
Sr	94	93		111	83
Y	95	95			83
Zr	95	95			85

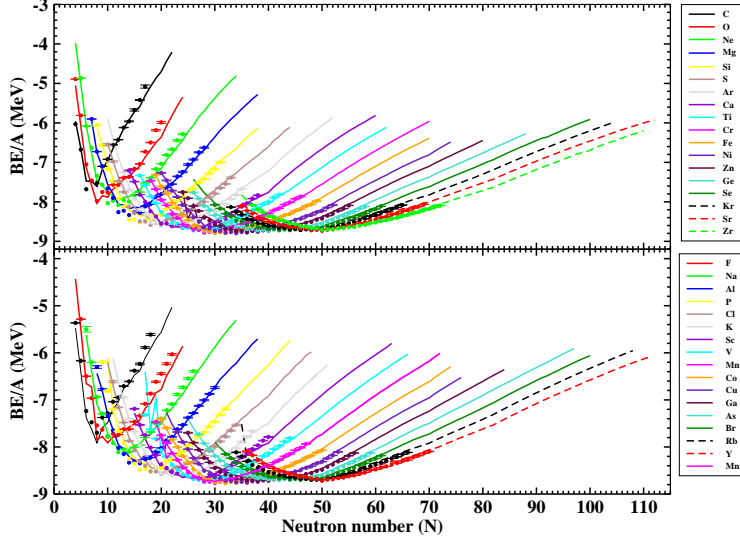


Figure 2: (color online) same as Fig. 1 but for NL3* parameterization.

izations. The highest value of BE/A for the nuclide corresponds to the maximum stability and is known as the most stable nucleus. Further, with an increase in the number of neutrons with a fixed value of Z so-called N/Z ratio increases, and corresponding BE/A monotonically decreases. This behaviour of the nuclides can be seen here in Fig. 1,2 and it must be generalized over the whole periodic table. Binding energy per particle obtained from the model and the available data from the experiment [54] is quite agreeable. However, the experimental data are not available up to the drip line region. Parabolic shapes are produced for every isotopic chain and the most bound isotopes lie on the deepest of the curve. Moreover, the two-neutron separation energies are estimated from the binding energies to explain the microscopic behaviour of the nuclei and other nuclear phenomena such as drip line, halo, or skin structure. The two-neutron separation energies are estimated using the following relation

$$S_{2n}(N, Z) = BE(N, Z) - BE(N - 2, Z). \quad (21)$$

The halo nucleus has the minimum value of S_{2n} on contrast a large value of neutron radius. Here, we have plotted the two-neutron separation energies for all considered isotopic series as a function of neutron number as given in

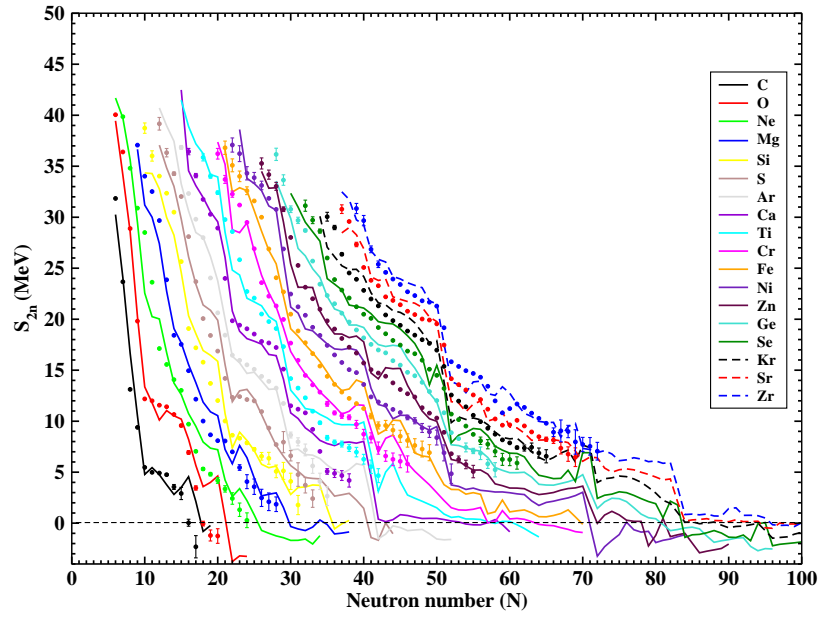


Figure 3: (color online) Two neutron-separation energy (S_{2n}) calculated using RMF theory with NL3 parameterization, is plotted as a function of neutron number for even- Z isotopes from C to Zr. Experimental data are represented by filled circles.

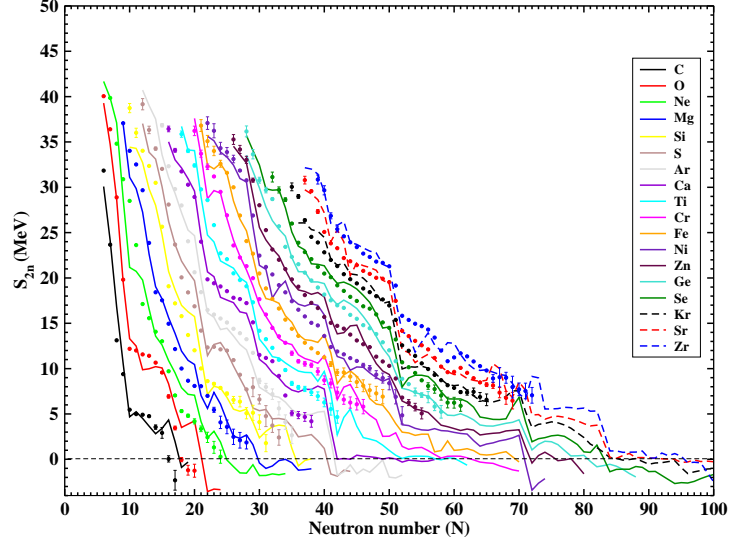


Figure 4: (color online) same as Fig. 3 but for NL3* parameterization.

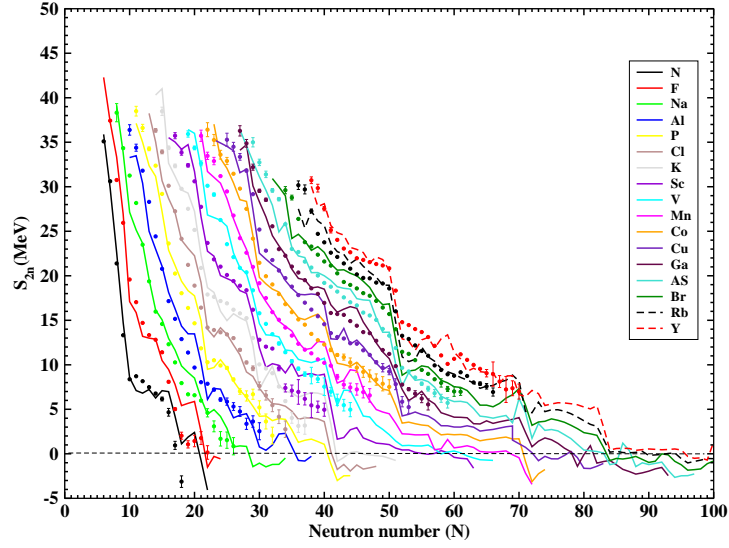


Figure 5: (color online) Same as Fig. 3 but for odd- Z isotopes from C to Zr.

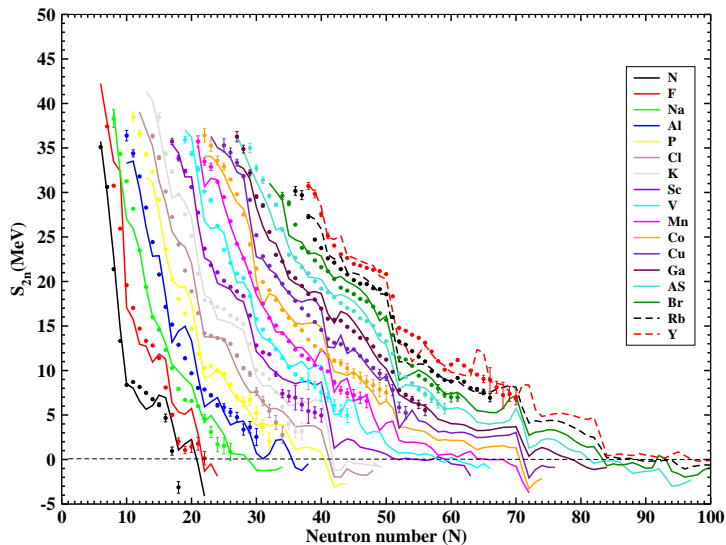


Figure 6: (color online) Same as Fig. 5 but for NL3* parameterization.

figures 3 to 6. On the basis of S_{2n} , the drip line nucleus is anticipated over the entire chain of isotopes. For instance, the relativistic continuum Hartree-Bogolubov (RCHB) theory reports the drip line nucleus to be ^{30}O [55], but our RMF with NL3 and NL3* marks ^{29}O as a drip nucleus, whereas the experimentally observed nucleus is ^{26}O . The drip line isotope for C is predicted as ^{24}C within RCHB framework [56], where our results suggest as ^{23}C . Also, the last bound isotope for Ca is predicted as ^{72}Ca within RCHB [55], HFB [57], SHF [58, 59] methods and our result predicts ^{73}Ca and ^{71}Ca for NL3 and NL3* parameterizations, respectively. In the case of Ni, ^{100}Ni is predicted as a drip nucleus with RCHB [55] while present calculations suggest as ^{98}Ni is the drip line nucleus with neutron number $N = 70$ within both parameterizations. This $N = 70$ has appeared here as a semimagic number. Moreover, both the parameterizations produce consistent results with each other. The disparities, in some cases, between RMF and RCHB are arises due to exclusion of continuum states in BCS pairing approximation within RMF(NL3/NL3*) framework.

Here, in Table 4, we have enlisted the possible neutron number for the two-neutron drip line nuclei in this work and a comparison is established between our work and the predictions of spherical RCHB [7] with

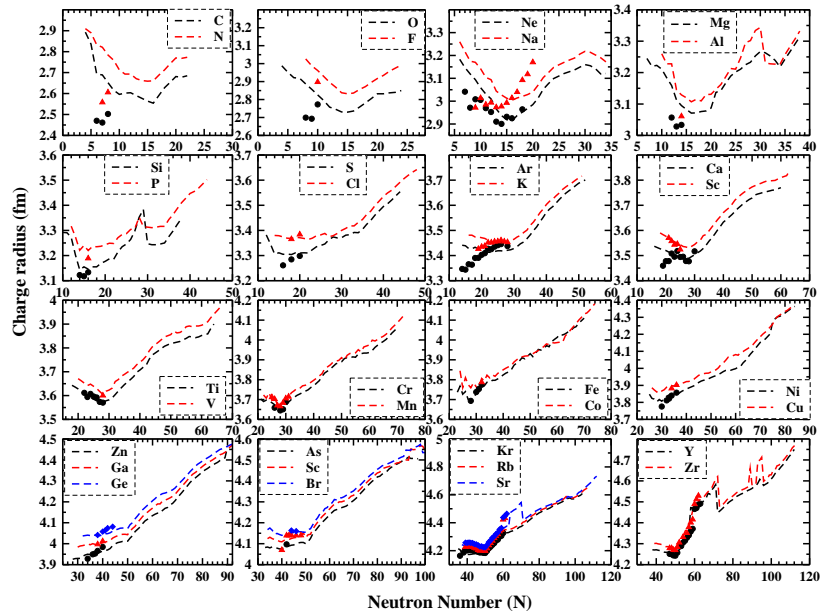


Figure 7: (color online) The charge radius (r_c), calculated using RMF theory with NL3 parameterization, is plotted as a function of neutron number from C to Zr isotopes. Experimental data are represented by filled circles, triangles and diamonds.

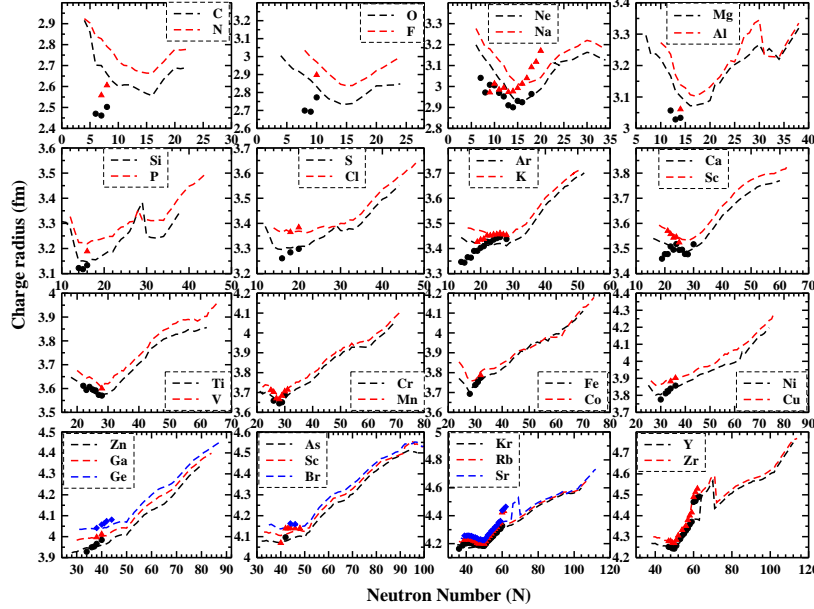


Figure 8: (color online) Same as Fig. 7 but for NL3* parameterization.

PC-PK1 parameterization and macro-microscopic finite range droplet model (FRDM) [60]. The two-neutron drip lines for C, N, and O have also been determined using experimental two-neutron separation energies and also listed in one of the columns of Table 4. The two neutron drip line found in this work lies nearby to the available experimental evaluation but differs largely from the prediction of FRDM and spherical RCHB [7]. Therefore, reliable prediction of drip line is a matter of discussion in nuclear physics because its predictions are not only model but interaction dependent also.

In the context of radii, the charge radius produced by RMF(NL3) or RMF(NL3*) matches with RCHB predictions [7]. For example, for ^{28}O , the charge value is $r_c = 2.903$ fm within RCHB whereas 2.832 fm and 2.837 fm for RMF(NL3) and RMF(NL3*). Also, for ^{30}F , $r_c = 2.977$ fm within RCHB whereas 2.934 fm and 2.937 fm for present NL3 and NL3* interactions. For ^{49}Si nucleus, the value of r_c within RCHB is 3.332 fm on the other hand charge radius comes out to be 3.275 fm and 3.272 fm in present RMF calculations. In case of ^{95}Fe , the continuum method produces the charge radius around $r_c = 4.149$ fm, whereas BCS mean-field predicts as 4.097 fm and 4.096 fm. In the same way, for ^{135}Zr the amount of charge radius $r_c = 4.643$ fm for

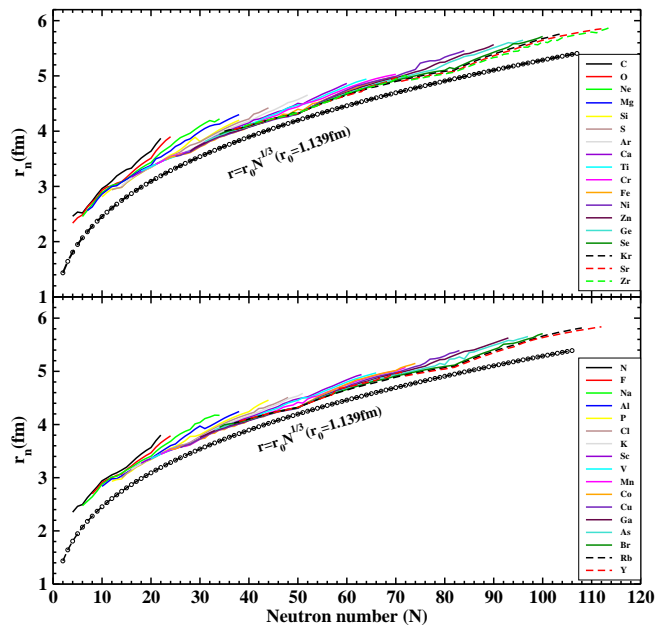


Figure 9: (color online) The root mean square neutron radii, calculated using RMF theory with NL3 parameterization, is plotted as a function of neutron number for even- Z isotopes (upper panel) and for odd- Z isotopes (lower panel) from C to Zr.

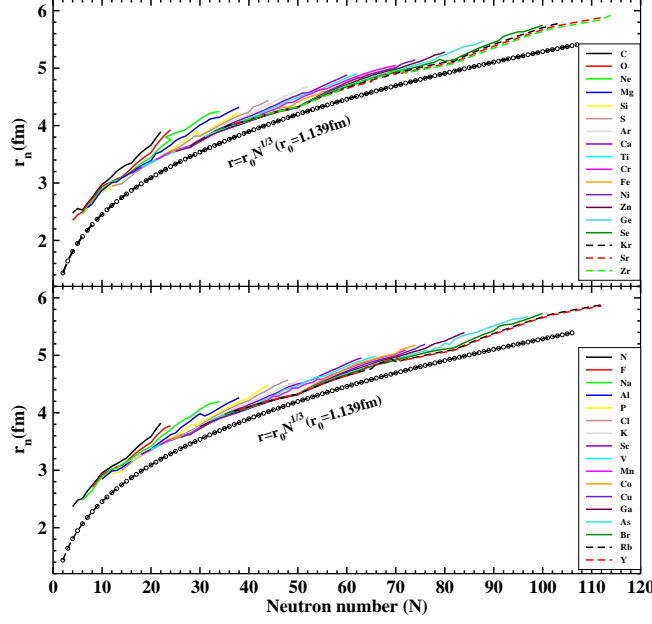


Figure 10: (color online) Same as Fig. 9 but for NL3* parameterization.

continuum method and 4.592 fm and 4.589 fm for mean-field method in present calculations. Therefore, it is evident that the continuum method like RCHB produces the upper limit of charge radius than RMF (NL3/NL3*) predictions.

It is worth mentioning that a nucleus may have any possible configuration from three kinds; oblate or spherical or prolate. Nuclei optimize the energy corresponding with their shape configuration. Sometime nucleus exists in two or more possible shape configurations with almost the same energies which is termed as shape coexistence in literature. Here, the shape of the nuclei for considered isotopic series comes out to be spherical or prolate by examining the deformation parameter. There is no such oblate shaped. Even some of the drip line nuclei have large prolate shaped and these results are consistent with experimental values [61]. For example, ^{34}Ne , ^{39}Na , and ^{41}Mg drip line nuclei have a large value of $\beta_2 \approx 0.4$ within both parameterization and therefore predict a large deformed shape. Other than large or mild prolate shaped, drip line nuclei have a spherical configuration. Moreover, both the interactions produce consistent results with each other.

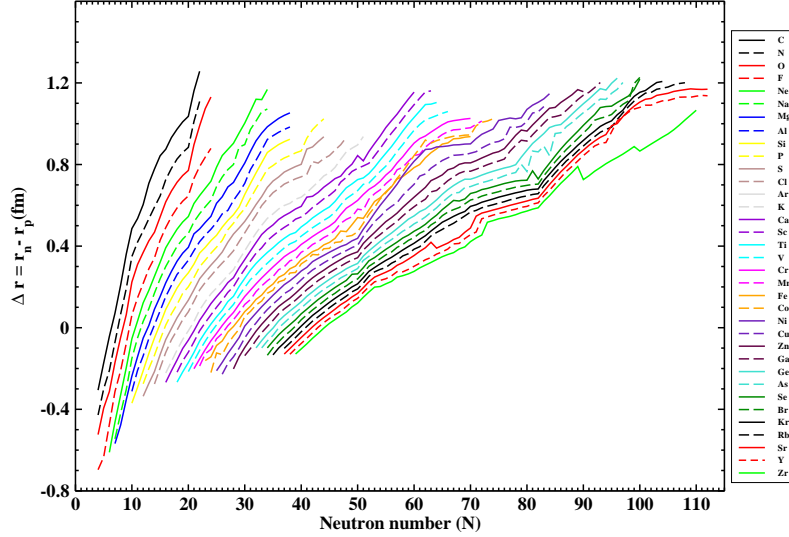


Figure 11: (color online) Neutron skin-thickness from β stable to drip line region, calculated using RMF theory with NL3 parameterization, is given as a function of neutron number for nuclei from C to Zr. Even- Z isotopes are represented by solid line whereas dashed line is used for showing the odd- Z isotopes.

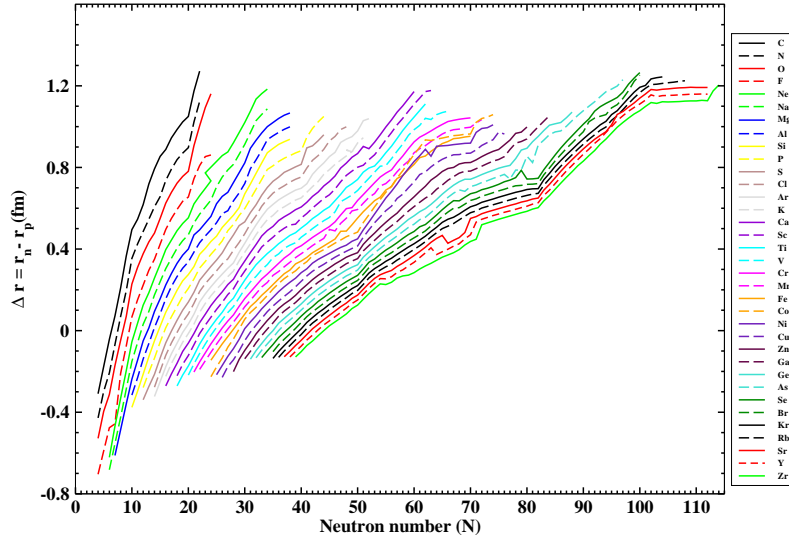


Figure 12: (color online) Same as Fig. 11 but for NL3* parameterization.

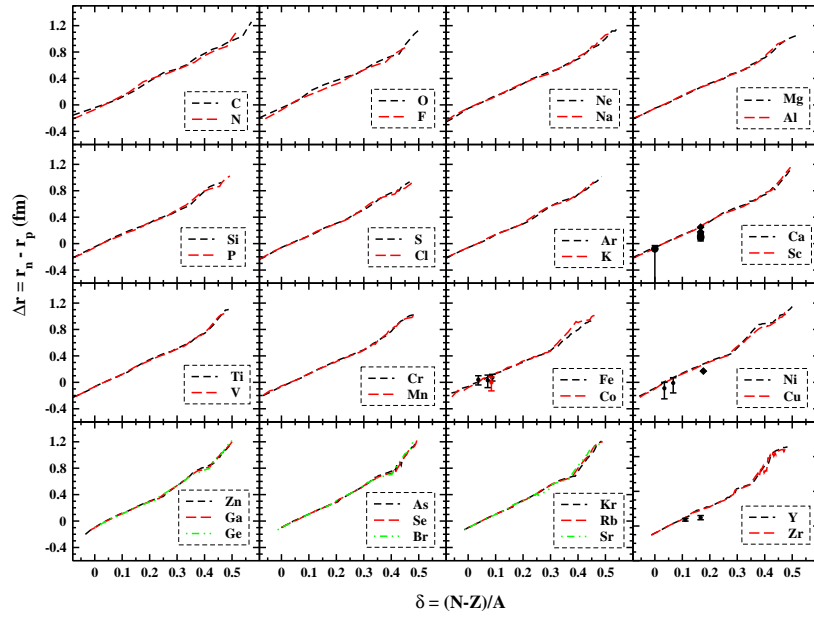


Figure 13: (color online) Neutron skin-thickness from β stable to drip line region, calculated using RMF theory with NL3 parameterization, is plotted as a function of asymmetry parameter ($\delta = N - Z/A$) for the nuclei from C to Zr. Available experimental data are represented by filled circles with error bars. Available earlier theoretical predictions are symbolized by diamonds or triangles.

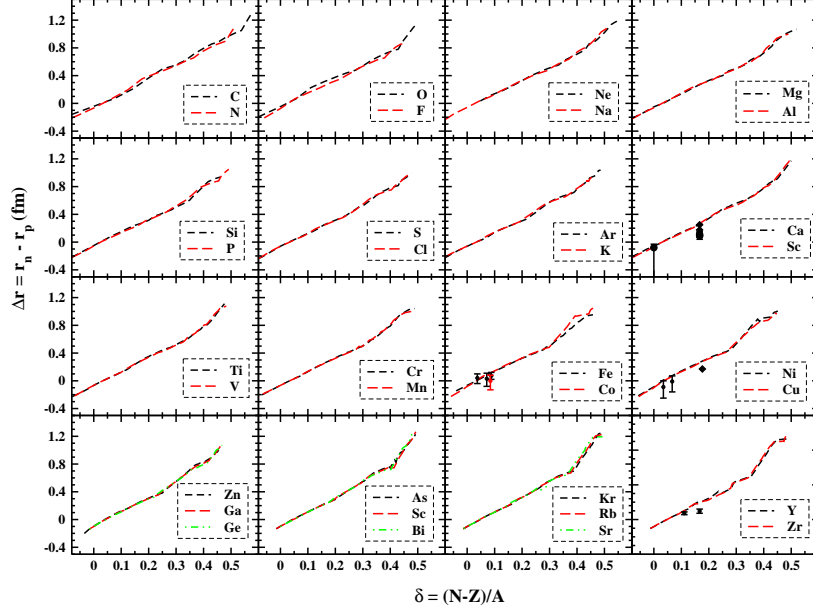


Figure 14: (color online) Same as Fig. 13 but for NL3* parameterization.

Separation energy is supposed to be the first signature in distinguishing the magic numbers for an isotopic series. The extended shell gaps in the single-particle energy levels are identified as magic numbers in nuclei. This suggests an abrupt fall in neutron separation energy indicates the signature of the neutron magic number. In general, the separation energy decreases smoothly with increasing neutron numbers. But, there are found to be kinks at $N = 20, 40, 50, 70,$ and 82 in figures 3,4, 5 and 6, which are all traditional magic or semimagic numbers. However, neutron magic number $N = 28$ is no longer seen and disappear in all isotopes. The in held spin-orbit splitting in RMF formalism gives the strength to this model to reproduce the experimental magic number.

3.2 Charge, neutron radii and neutron skin-thickness

The charge radius and the way neutrons are distributed in the nucleus are the fundamental properties to find the dimension of the nucleus. Experimentally, charge radii for stable nuclei are obtained through electron scattering with a high level of accuracy. Such studies provide information about a few

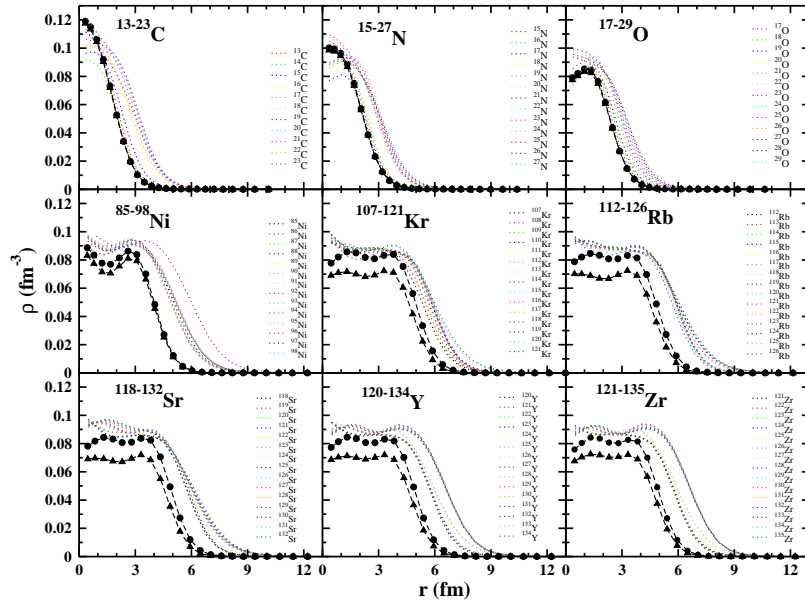


Figure 15: (color online) Neutron density distributions for rich skin candidates (C, N, O, Ni, Kr, Rb, Sr, Y and Zr isotopic chain) as a function of radial parameter (r) is given. Neutron (line with filled circles) and proton densities (line with filled triangles) for stable cases are also plotted. These densities are calculated using RMF theory with NL3 parameterization.

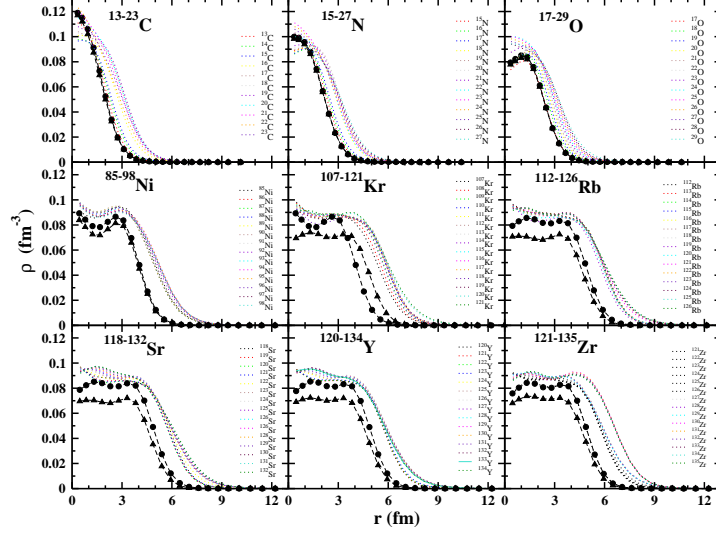


Figure 16: (color online) Same as Fig. 15 but for NL3* parameterization.

of the foremost principal properties of nuclei, such as size, surface thickness, shell structure, and distribution of nucleons. Contrary to the nuclear charge densities, we still have a circumscribed knowledge about neutron densities. And therefore, in nuclear physics, determining r_n of a nucleus is a problem of fundamental significance. In order to illustrate the size and probably halo/skin structure of the considered isotopic series, rms charge, rms neutron radii, and neutron skin thickness are calculated within the RMF theory from β stable to the neutron drip line region and plotted in figures 7-10. It is evident from Figs 7,8 that the r_c is smaller for the stable isotopes in comparison to the isotopes lie near proton or neutron drip line regions. It is the point in the curve, where asymmetry and Coulomb terms are in extremely balancing positions, giving an extremely stable isotope. The charge radius is seen as least for ^{28}Si with $N = 14$, owing to the shell effect and formed the most stable nucleus among Si isotopic chain. Before and after $N = 14$ the charge radius increases with changing in neutron number. This trend of r_c is followed by all considered isotopes as manifested in Figs. 7,8. The abrupt increase in r_c leads to changes in the shape of the isotopes than previous ones. Calculated theoretical values of charge radius for these isotopes agree well with available experimental data [28]. However, a deviation for light nuclei is observed but an excellent consistency between our theoretical results and

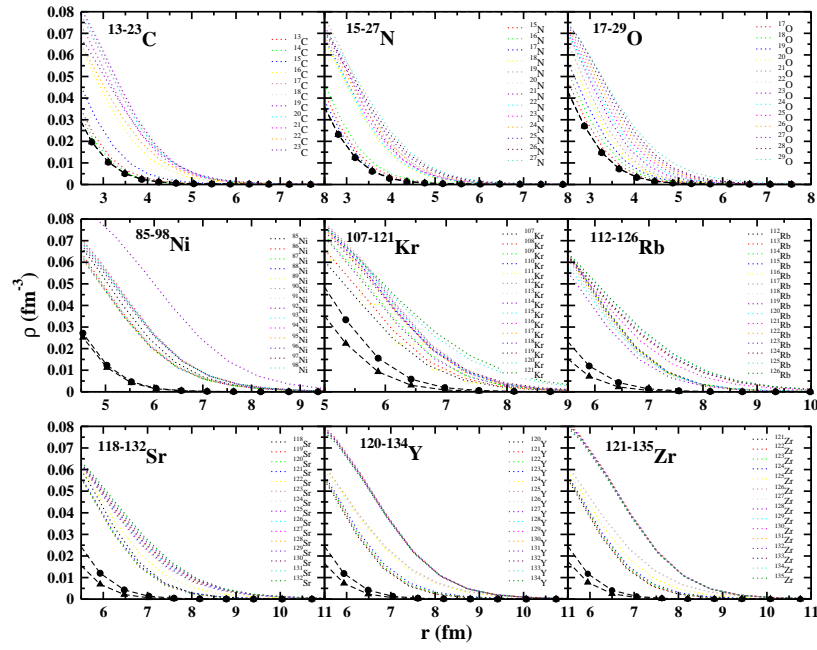


Figure 17: (color online) Neutron density distributions for said rich skin candidates but for peripheral region in view to guide the long tails. These densities are calculated using RMF theory with NL3 parameterization.

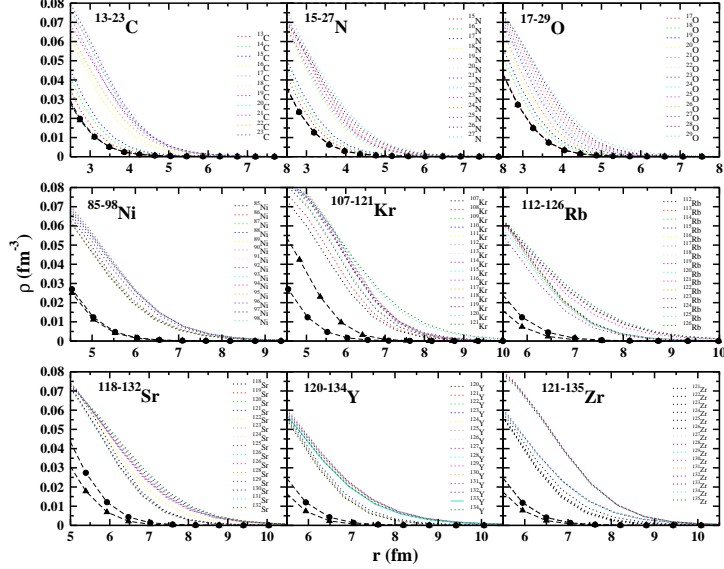


Figure 18: (color online) Same as Fig. 17, but for NL3* parameterization.

experimental data is noticed for the medium mass range of nuclei.

In Figs. 9,10 the determined rms neutron radii are plotted against the number of neutrons. It is fascinating to see that r_n follows the stability curve nicely for β stable region and makes the deviation for exotic drip line region. The stability curve is computed by the empirical formula $r = r_0 N^{1/3}$. The sharp increase in the slope of r_n at the drip line region indicates the larger neutron radius than the normal trend and probably skin structure shall appear. A deviation of r_n from empirical prediction is seen for the isotopes C, N, O, Ni, Kr, Sr, Rb, Y, and Zr in the exotic mass region. Of course, these rises in r_n are due to valence neutrons adjusted to nuclei and forming the skin/halo structure. This fact strongly supports the possibility for the existence of the neutron skin/halo in exotic C, N, O, Ni, Kr, Sr, Rb, Y, and Zr isotopes. The outcomes of these results are in favour of earlier predictions [55, 62–65]. However, deviation of r_n for C, N, O are under suspicion because RMF model doesn't appear well in case of light mass nuclei due to its mean-field nature [66].

In figures 11, 12, we show the neutron skin thickness as a function of neutron number N for the considered isotopic chains. The magnitude of skin thickness increasing systematically with the number of neutrons within

the isotopes. The gradual increment in the neutron skin may be described as the redistribution of the nucleons with the additament of neutrons to a stable nucleus. The slope of the thickness is larger for some isotopes, for example, C, N, O, Ni, Kr, Rb, Sr, Y, and Zr due to their halo nature as predicted earlier by authors [55, 62–65]. It is to be noted that Ni with $N > 50$ and Kr, Rb, Sr, Y, Zr isotopes with $N > 82$ show a sharp increase in skin thickness and a large decrease in two neutron separation energies. For example, Ni with $N = 50$ has the value of $S_{2n} = 9.468$ MeV while this amount goes to 3.031 MeV at $N = 52$. Neutron skin thickness varies in magnitude from stable to neutron drip line region. Considered neutron-rich nuclei show the maximum skin thickness of the order of 0.9 fm. The thickness particularly for the drip line nucleus is framed in Table 2 and Table 3. Moreover, the skin thickness is also represented as a function of the asymmetry parameter ($\delta = N - Z / N + Z$) in Figs. 13, 14. This graph shows the correlation of skin thickness with the asymmetry parameter. The trends of the set of data indicate an approximate linear dependency of neutron-skin thickness to the relative neutron excess of the nucleus. It is demonstrated that our results match very well with available experimental data [67, 68] within the error bars, and existing theoretical extractions [69–72]. Skin for ^{48}Ca has been reported as $\Delta r = (0.176 \pm 0.018)$, $(0.12-0.15)$, (0.249 ± 0.023) with density functional theory [69], ab initio calculations [70], dispersive optical model [71], respectively. The present value of the skin for ^{48}Ca is found to be 0.245 fm which satisfies the earlier predictions [69–71, 73].

It is evident from Table 1 that there is no such difference within both interactions and NL3* is just the improved version of NL3 force. As we have already mentioned in the first section that the neutron skin thickness is strongly correlated with density dependence of neutron symmetry energy at saturation [16–21, 24–28]. Not only this, the slope of the symmetry energy which is expected to be the cornerstone of drip line, masses, densities, and skin thickness of neutron-rich nuclei [74]. Here, the both forces (NL3 and NL3*) have almost similar values of slope parameters i.e. $L = 118.6$ MeV and $L = 122.63$ MeV for NL3 and NL3* respectively, and therefore both forces produce almost identical drip lines and neutron skin thickness.

The predicted neutron skin for exotic nuclei might be used to simulate the symmetry energy for the neutron-rich matter. The slope parameter shall be varied with variable skin thickness. However, there are uncertainties in neutron skin produced by different models and it is a model dependent quantity. The results on skin thickness may also be used for determining or extracting

the isovector part from nucleon-nucleon interaction. The isospin behaviour of nucleon interaction exhibits more precisely from heavy nuclei such as ^{208}Pb . Such nuclei have a large inequality in neutron and proton number and therefore show the existence of symmetry energy. So, very next we shall look for the skin of largely unequal heavy nuclei. Further, the skin structure shall be viewed by investigating the density distributions. In the very next subsection, we shall look at the density profile for neutron skin candidates.

3.3 Density profile

The variance of densities with internucleon separation (r) gives the insight of nucleons distributions inside the nuclei from the center to the surface region. The central part of density is meaningful for characterizing the bubble or semi-bubble type structure [75–77], whereas the tail part has signified as far as halo and skin structure is concerned. Here, we plot the densities for the designated neutron-rich nuclei, showing the anomalous behaviour of r_n in comparison to the empirical trend. The isotopes, for example, C, N, O, Ni, Kr, Rb, Sr, Y, and Zr are used to plot the neutron density to look for the tails as given in figures 15-18. We witness a tail is increasing for O, Ni, Kr, Rb, Sr, Y, and Zr in comparison to other nuclei with increasing neutron numbers. This may be understood that the added neutrons redistribute the whole shell structure of the nucleus and as a result, extended density distribution is formed. Neutron and proton densities for stable nuclides (e.g. ^{12}C , ^{14}N , ^{16}O , ^{58}Ni , ^{84}Kr , ^{85}Rb , ^{88}Sr , ^{89}Y , ^{90}Zr) are also plotted for the sake of references and comparisons. Exotic nuclei of these isotopes have a long tail indicating the skin structure. It is evident from Figs. 17 and 18 the fall of peripheral density at $r = 4$ fm is seen for stable nuclei of ^{12}C , ^{14}N , ^{16}O but the peripheral region goes on increasing with the increase in the number of neutrons and the end of density at $r = 6$ fm. In the same fashion, for medium mass nuclei Ni, Kr, Rb, Sr, Y, and Zr, the peripheral density ends at $r = 10$ fm for neutron-rich exotic nuclei instead of $r = 7$ fm for stable cases. This gradual increase in the amount of peripheral region due to the excessive number of neutrons is responsible for a large amount of neutron skin thickness. In general, the density profile shows a noteworthy decent expansion of neutron density when contrasted with proton density at the tail part of considered nuclei. The extension is equal to or more than 2 fm in these cases, which supports the strong skin structure.

4 Summary and conclusion

The charge radii, neutron radii, and neutron skin thickness over a series of the isotopic chains of isotopes C to Zr ranging from their β stability line to the two-neutron drip line have been explored. Theoretical calculations are made from axially deformed solution of Lagrange equations. To understand the size of the isotopes, the charge radii are analyzed. Binding energy per particle is plotted to expose the maximum stability of the nuclides. To understand the skin structure, neutron radii are plotted as functions of neutron number and compared with empirical estimations ($r = r_0 N^{1/3}$). Calculated theoretical results are contrasted with accessible experimental data as well as different theoretical predictions and a satisfactory agreement is observed. We also estimated the two-neutron separation energy by which drip line nuclei are marked and traditional magic numbers are seen. BCS pairing scheme has some limitation in drip line region and therefore for more convincing results a better pairing approximation is needed to care of continuum states. To examine the skin structure more precisely, neutron density distribution is analyzed by plotting the density. The density profile shows a remarkable good extension of neutron density as compared to proton density at the tail part of considered nuclei. Finally, neutron skin thickness is observed for the whole considered isotopic series and a maximum amount 1.053 fm is noticed for ^{134}Y (NL3*). The separation energies, radii, and densities are considered to be the significant quantities in order to examine the halo nuclei. In some cases, large diffused densities are encountered, which may lead to halo structure in those exotic neutron-rich nuclei. For example, ^{134}Y is highly a diffused nucleus with extremely large Δr , which implies that it may be a halo nucleus. Further, cross-sectional studies on theoretical and experimental basis are needed to get a more clear picture of the existence of a halo structure.

Acknowledgements

One of the author(UR) would like to thank University Grant Commission for providing UGC-SRF fellowship.

References

- [1] I. Tanihata, J. Phys. G: Nucl and Part. **22**, 157 (1996).
- [2] C. J. Horowitz and J. Piekarewicz, Phys. Rev. Lett. **86**, 5647 (2001).
- [3] C. J. Horowitz and J. Piekarewicz, Phys. Rev. C **64**, 062802(R) (2001).
- [4] G. Hagen et. al., Nat. Phys. **12**, 186 (2016).
- [5] S. kaufmann et. al., Phys. Rev. Lett. **124**, 132502(2020).
- [6] S. E. Agbemava, A. V. Afanasjev, D. Ray and P. Ring, Phys. Rev. C **89**, 054320(2014).
- [7] X. W. Xia et.al., At. Data and Nucl. Data Tables **121**, 1 (2018).
- [8] K. Zhang et. al., arXiv:2001.06599v1(2020).
- [9] I. Tanihata, et al., Phys. Lett. B **289**, 261 (1992).
- [10] G. D. Alkhozov, et al., Phys. Rev. Lett. **78**, 2313 (1997).
- [11] B. Alex Brown, Phys. Rev. Lett. **119**, 122502 (2017).
- [12] B. Alex Brown et. al., Phys. Rev. C **79**, 035501 (2009).
- [13] M. Centelles et. al., Phys. Rev. Lett. **102**, 122502 (2017).
- [14] Liu Min, Wang Ning, LI Zhu Xia and Wu Xi. Zhen, Chin. Phys. Lett. **23** 804 (2006).
- [15] M. Warda, M. Centelles, X. Viñas, and X. Roca Maza, Acta Phys. Pol. B **43**, 209 (2012).
- [16] Lie-Wen Chen, Che Ming Ko and Bao-An Li, Phys. Rev. C **72**, 064309 (2005).
- [17] B. Alex. Brown, Phys. Rev. Lett. **85**, 5296 (2000).
- [18] C. J. Horowitz and J. Piekarewicz, Phys. Rev. Lett. **86**, 5647 (2001); Phys. Rev. C **66**, 055803 (2002).
- [19] S. Typel and B. Alex Brown, Phys. Rev. C **64**, 027302 (2001).

- [20] R. J. Furnstahl, Nucl. Phys. A **706**, 85 (2002).
- [21] S. Karataglidis, K. Amos, B. Alex Brown, and P. K. Deb, Phys. Rev. C **65**, 044306 (2002).
- [22] S. Abrahamyan et al., Phys. Rev. Lett. **108**, 112502 (2012).
- [23] M. Thiel, C. Sienti, J. Piekarewicz, C. J. Horowitz and M. Vanderhaeghen J. Phys. G: Nucl. Part. Phys. **46** 093003 (2019).
- [24] T. Sil, S. K. Patra, B. K. Sharma, M. Centelles and X. Viñas, Phys. Rev. C **69**, 044315 (2004).
- [25] B. K. Agarwal, S. K. Dhiman, Phys. Rev. C **73**, 034319 (2006).
- [26] C. Mondal et. al., Phys. Rev. C **93**, 064303 (2016).
- [27] P. -G. Reinhard, W. Nazarewicz, Phys. Rev. C **93**, 051303(R) (2016).
- [28] I. Angeli, K. P. Marinova, At Data Nucl. Data Tables **90**, 69 (2013).
- [29] A. W. Steiner, M. Prakash, J. M. Lattimer and P. J. Ellis, Phys. Rep. **411**, 325 (2005).
- [30] J. Carriere, C. J. Horowitz, and J. Piekarewicz, Astrophys. J. **593**, 463 (2003).
- [31] S. F. Ban, J. Li, S. Q. Zhang, H. Y. Jia, J. P. Sang and J. Meng, Phys. Rev. C **69**, 045805 (2004).
- [32] J. Meng, H. Toki, S. G. Zhou, S. Q. Zhang, W. H. Long, and L. S. Geng, Prog. Part. Nucl. Phys. **57**, 470 (2006).
- [33] B. D. Serot, Rep. Prog. Phys. **55**, 1855 (1992).
- [34] Y. K. Gambhir, P. Ring, and A. Thimet, Ann. Phys. (N.Y.) **198**, 132 (1990).
- [35] P. Ring, Prog. Part. Nucl. Phys. **37**, 193 (1996).
- [36] B. D. Serot and J. D. Walecka, Adv. Nucl. **16**, 1 (1986).
- [37] J. Boguta, and A. R. Bodmer, Nucl. Phys. A **292**, 413 (1977).

- [38] H. L. Yadav et al. Int. J. Mod. Phys. E **13**, 647 (2004).
- [39] S. K. Patra, Raj K. Gupta and W. Greiner Int. J. Mod. Phys. E **06**, 641 (1997).
- [40] G. A. Lalazissis, S. Raman, Phys. Rev. C **58**, 1467 (1998).
- [41] M. M. Sharma, G. A. Lalazessis. W. Hillebrandt and P. Ring, Phys. Rev. Lett. **72**, 1431 (1994).
- [42] L. S. Warrier and Y. K. Gambhir, Phys. Rev. C **49**, 871 (1994).
- [43] A. Ekstrom et. al., Phys. Rev. C **91**, 051301(R) (2015).
- [44] B. S. Hu et. al., Phys. Rev. C **94**, 014303 (2016).
- [45] G. A. Lalazissis, J. Konig and P. Ring, Phys. Rev. C **55**, 540 (1997).
- [46] G. A. Lalazissis, S. Karatzikos, R. Fossion, D. Pena Arteaga, A. V. Afanasjev and P. Ring, Phys. Lett. B **671**, 36 (2009).
- [47] M. Dutra, Phys. Rev. C **90**, 055203 (2014).
- [48] F. Grill, H. Pais, C. Providência, I. Vidaña and S. S. Avancini, Phys. Rev. C **90** 045803 (2014).
- [49] Y. K. gambhir, P. Ring, A. Thimet Ann. of Phys. **198**, 132 (1990).
- [50] S. K. Patra, C. R. Praharaaj, Phys. Rev. C **44**, 2552 (1991).
- [51] D. G. Madland, R. J. Nix, Nucl. Phys. A **476**, 1 (1988).
- [52] S. K. Patra, M. Del Estel, M. Centelles and X. Vinas, Phys. Rev. C **63**, 024311 (2001).
- [53] A. A. Usmani, S. Afsar Abbas, U. Rahaman, M. Ikram and F. H. Bhat, Int. J. Mod. Phys. E **27**, 1850060 (2018).
- [54] Meng Wang, G. Audi, F.G. Kondev, W.J. Huang, W.J. Huang, and Xing Xu, Chinese Physics C **41** (2017) 030003.
- [55] J. Meng et. al., Phys. Rev. C **65**, 041302(R)(2002).

- [56] W. Poschl, D. Vretenar, G. A. Lalazissis, and P. Ring, Phys. Rev. Lett. **79**, 3841 (1997).
- [57] S. A. Fayans, S. V. Tolokonnikov and D. Zawischa, Phys. Lett. B **491**, 245 (2000).
- [58] Im Soojae and J. Meng, Phys. Rev. C **61**, 047302 (2000).
- [59] I. Hamamoto, H. Sagawa and X. Z. Zhang, Phys. Rev. C **64**, 024313 (2001).
- [60] P. Moller, A. Sierk, T. Ichikawa, H. Sagawa, At. Data and Nucl. Data Tables **109**, 1 (2016).
- [61] S. Raman, C. W. Nestor Jr, and P. Tikkanen, At. Data and Nucl. Data Tables **78**, 1 (2001).
- [62] J. Meng et. al., Phys. Rev. C **74**, 054318 (2006).
- [63] S. -Q. Zhang, J. Meng, S. -G, Zhou and J. -Y. Zeng, Chin. Phys. Lett. **19**, 312 (2002).
- [64] J. Meng, H. Toki, J. Y. Zeng, S. Q. Zhang, and S.-G. Zhou, Phys. Rev. C **65**, 041302(R) (2002).
- [65] J. Meng and P. Ring, Phys. Rev. Lett. **80**, 460 (1998).
- [66] S. K. Patra, Int. J. Mod. Phys. E **2**, 471 (1993).
- [67] J. Jastrzebski, A. Trzcinska, P. Lubinski, Int. J. Mod. Phys. E **13**, 343 (2004).
- [68] E. Friedman, Nucl. Phys. A **896**, 46 (2012).
- [69] J. Pickarewicz, et. al. Phys. Rev. C **85**, 141302 (2012).
- [70] G. Hagen et.al., Nat. Phys. **12**, 186 (2016).
- [71] M. H. Mahzoon, M. C. Atkinson, R. J. Charity, W. H. Dickhoff, Phys. Rev. Lett. **119**, 222503 (2017).
- [72] X. Roca-Maza et.al., Phys. Rev. C **92**, 064304 (2015).

- [73] V. Thakur and S. K. Dhiman, Nucl. Phys. A **992**, 121623 (2019).
- [74] X. Roca-Maza, M. Centelles, X. Viñas, M. Warda, Phys. Rev. Lett. **106**, 252501 (2011).
- [75] M. Grasso et al., Phys. Rev. C **79**, 034318 (2009).
- [76] E. Khan. et al., Nucl. Phys. A **800**, 37 (2008).
- [77] S. K. Singh, M. Ikram, S. K. Patra, Int. J. Mod. Phys. E **22**, 1350001 (2013).